

Article

The Optimization of NiO Doping, Thickness, and Extension in kV-Class NiO/Ga₂O₃ Vertical Rectifiers

Chao-Ching Chiang ¹, Jian-Sian Li ¹, Hsiao-Hsuan Wan ¹, Fan Ren ¹ and Stephen J. Pearton ^{2,*}

¹ Department of Chemical Engineering, University of Florida, Gainesville, FL 32611, USA; cchiang@ufl.edu (C.-C.C.); jiansianli@ufl.edu (J.-S.L.); hwan@ufl.edu (H.-H.W.); ren@che.ufl.edu (F.R.)

² Department of Material Science and Engineering, University of Florida, Gainesville, FL 32611, USA

* Correspondence: spear@mse.ufl.edu

Abstract: Ga₂O₃ heterojunction rectifiers have emerged as a novel candidate for various power conversion applications by using NiO as the solution on the p-type side. In this work, the optimized design of high-breakdown (1–7 kV), vertical geometry NiO/Ga₂O₃ rectifiers was examined using the Silvaco TCAD simulator to determine the electric field distribution for different NiO parameters. The doping concentration (10¹⁷–10¹⁹ cm⁻³), thickness (10–70 nm) of the guard ring, and its extension beyond the anode (0–30 μm) are all important in determining where the device breakdown occurs. Spatially, this can vary from the edge of the bilayer NiO extension to directly at the periphery of the top contact, consistent with experimental results. This transition phenomenon is proven to be correlated with the depletion effect by monitoring the depletion width when ramping up the bias and the doping concentration. The breakdown voltage was also calculated as a function of NiO top and bottom layer thicknesses and the doping concentration under different critical breakdown fields, where the latter is determined by the material quality of the drift layer.

Keywords: TCAD simulation; NiO; Ga₂O₃ rectifiers; high breakdown



Citation: Chiang, C.-C.; Li, J.-S.; Wan, H.-H.; Ren, F.; Pearton, S.J. The Optimization of NiO Doping, Thickness, and Extension in kV-Class NiO/Ga₂O₃ Vertical Rectifiers. *Crystals* **2023**, *13*, 1124. <https://doi.org/10.3390/cryst13071124>

Academic Editor: Andreas Thissen

Received: 6 July 2023

Revised: 13 July 2023

Accepted: 18 July 2023

Published: 19 July 2023



Copyright: © 2023 by the authors. Licensee MDPI, Basel, Switzerland. This article is an open access article distributed under the terms and conditions of the Creative Commons Attribution (CC BY) license (<https://creativecommons.org/licenses/by/4.0/>).

1. Introduction

Ultra-wide bandgap semiconductors have captured the attention of researchers and scientists due to their exceptional properties and promising applications across various fields. Their wide energy bandgap, high breakdown voltage, remarkable thermal stability, and high carrier mobility make them ideal candidates for power electronics, optoelectronics, and high-frequency devices. As ongoing research advances the understanding and fabrication techniques of UWBG materials, their widespread integration into numerous technologies is expected, revolutionizing industries and shaping the future of electronics. Continued exploration of UWBG semiconductors will undoubtedly unlock their full potential and pave the way for exciting technological advancements.

Ultra-wide bandgap semiconductors, such as gallium nitride (GaN), aluminum nitride (AlN), and diamond, are attracting considerable attention in current scientific research. These materials possess energy bandgaps larger than 3 eV, distinguishing them from conventional wide bandgap semiconductors like silicon carbide (SiC) and gallium arsenide (GaAs). The unique properties of UWBG semiconductors make them highly desirable for applications where extreme performance is required. This article elucidates the reasons for the surge in scientific interest and potential applications of UWBG semiconductors.

Ultra-wide bandgap semiconductors exhibit extraordinary material characteristics that set them apart from traditional semiconductors. Their wide energy bandgap ensures minimal leakage currents, higher breakdown voltages, and superior thermal stability, making them suitable for high-temperature and high-power applications. Additionally, UWBG semiconductors possess exceptional carrier mobility, enabling fast switching speeds and high-frequency operation.

One significant area where UWBG semiconductors are gaining attention is power electronics. The high breakdown voltage and low on-resistance of UWBG materials make them ideal for power devices, such as transistors and diodes, capable of handling high voltages and currents. Their ability to operate at higher temperatures further enhances their utility in power electronic systems, where efficient and compact solutions are essential.

The unique material properties of UWBG semiconductors also make them well-suited for optoelectronic applications. The wide bandgap enables the emission and detection of light in the ultraviolet (UV) and deep UV regions, expanding the potential for advanced UV-light-emitting diodes (LEDs), photodetectors, and sensors. These devices find applications in areas such as water purification, sterilization, and biological analysis.

Ultra-wide bandgap semiconductors exhibit exceptional carrier mobility, enabling high-frequency operation in electronic devices. This property makes them attractive for applications in high-frequency and high-power electronics, such as radio frequency amplifiers, wireless communication systems, and radar technology. The potential for faster switching speeds and reduced energy losses in these devices paves the way for enhanced efficiency and performance.

The ultra-wide-bandgap semiconductor, Ga_2O_3 , has advantages over Si electronics in terms of the ability to achieve higher breakdown voltage and lower on-state resistance [1–9]. Recent demonstrations of the ability of $\text{NiO}/\beta\text{-Ga}_2\text{O}_3$ vertical geometry rectifiers to achieve excellent performance [9–24] and breakdown voltages in excess of 8 kV [7,25–27] has revitalized interest in the heterojunction approach to overcome the lack of a practical p-type doping capability for $\beta\text{-Ga}_2\text{O}_3$. Several groups have now demonstrated devices with breakdown voltage and on-state resistance beyond the 1D limit of both GaN and SiC, showing the increasing maturity of Ga_2O_3 power device technology [7,25]. These devices are intended for power conversion applications in the 1.2–20 kV range such as electric vehicles, solid-state transformers, data centers, motor control, photovoltaic inverters, other renewable energy conversion, and electric grid protection [1,3,4,6].

The advancement of ultra-wide bandgap power electronics based on Ga_2O_3 relies heavily on the integration of modelling and simulation techniques. These tools provide valuable insights into the material properties, device characteristics, and system-level performance, ultimately guiding the optimization of Ga_2O_3 -based power devices. Through enhanced scientific understanding and technological implementation, Ga_2O_3 -based power electronics hold great promise for revolutionizing various industries and enabling more efficient and sustainable power conversion systems. However, the realization of efficient Ga_2O_3 -based power devices requires a comprehensive understanding of the material's electrical, thermal, and structural properties, as well as the optimization of device designs. Modelling and simulation serve as indispensable tools in this endeavor.

Modelling and simulation aid in characterizing the fundamental material properties of Ga_2O_3 , such as band structure, carrier transport mechanisms, and defect states. By employing quantum mechanical simulations, researchers can investigate the electronic structure and energy band alignment, elucidating the impact of various dopants and crystal orientations on device performance. These insights guide material engineering efforts to enhance the electrical and thermal properties of Ga_2O_3 .

Modelling and simulation enable the exploration and optimization of device structures for Ga_2O_3 -based power electronics. Through finite element analysis and computational electromagnetics, researchers can simulate the electrical and thermal behavior of devices under various operating conditions. This enables the evaluation of device performance metrics such as breakdown voltage, on-resistance, switching speed, and thermal management. Moreover, simulations help identify potential failure modes and design strategies to mitigate them, enhancing device reliability. To further advance the scientific understanding and technological implementation of Ga_2O_3 -based power devices, the integration of modelling and simulation techniques becomes crucial. This article highlights the importance of modelling and simulation in unraveling the intricate characteristics and optimizing the performance of UWBG power devices, thus accelerating their deployment in numerous applications.

Modelling and simulation aid in identifying and mitigating performance limitations in Ga₂O₃-based power devices. By incorporating physical models, such as carrier scattering and trapping, researchers can accurately predict device characteristics, including dynamic behavior, transient response, and switching losses. These simulations facilitate the optimization of device architectures, material compositions, and fabrication techniques to achieve higher efficiency, power density, and reliability.

Modelling and simulation play a vital role in the integration and scaling of Ga₂O₃-based power devices. Through simulations, researchers can study the impact of parasitic capacitances, inductances, and resistances, enabling the design of optimal circuit layouts and packaging configurations. Furthermore, simulations aid in predicting the behavior of Ga₂O₃ devices in complex power system scenarios, allowing for seamless integration into practical applications, such as renewable energy systems, electric vehicles, and aerospace electronics.

The application of modelling and simulation expedites the development cycle of Ga₂O₃-based power devices. By reducing the reliance on iterative experimental prototypes, simulations help in narrowing down the design space and guiding researchers towards optimal device architectures, material choices, and process parameters. Consequently, this accelerates the time-to-market for Ga₂O₃-based power electronics, fostering their commercial adoption and facilitating technological advancements.

An optimized edge termination design is required to achieve the full potential of Ga₂O₃ and obtain breakdown voltages near its theoretical limit by avoiding field crowding and early breakdown. For example, the rectifiers fail at contact edges under high reverse bias voltages via the formation of deep pits, while under forward bias, there is the introduction of cracking along crystallographic directions and even de-lamination of the epitaxial layer from the substrate via the high thermal and mechanical stresses developed at high forward current [28–30]. Transmission electron microscopy showed that the preferred direction of cracking was along (200) lattice planes. In addition, crack propagation and stacking faults lay on the same lattice planes, suggesting that the existence of stacking faults might help initiate cracking under mechanical loading. The critical field, E_C , is defined as the maximum electric field that leads to avalanche breakdown in a 1D analytical model. The breakdown voltage of a rectifier, V_B , is given by the relation:

$$V = \epsilon E_C^2 / 2eN_D \quad (1)$$

where ϵ is the permittivity, e is the electronic charge, and N_D is the doping density in the drift region. Previous simulations have found that the wider the total width of the p-NiO, the larger the on-state resistance, and the lower the reverse leakage current will be under a constant doping concentration in the NiO [8]. At a constant total width of the NiO, optimized p-type doping can enhance the breakdown voltage. However, there is still much to understand in terms of optimizing the design of NiO/Ga₂O₃ heterojunction rectifiers to take full advantage of the role of the NiO in providing a p-type layer but also to be used for edge termination.

In this paper, we present an optimized design for the edge termination with a strong agreement between theoretical and experimental data using the proper choices of the parameters in the NiO layers forming the p-side of the heterojunction, which is also utilized as a guard ring. Without this edge termination, early breakdown will occur at the edge of the anode due to field crowding at high blocking voltages. The thickness, doping concentration, and extension beyond the anode are varied within the simulation and compared to experimental data. We calibrated the basis of the simulations with real experimental data [15,25–27], as shown below, but the main part of the manuscript is on the simulations themselves, which are designed to allow for the design and optimization of the next generation of rectifiers with an even higher performance.

2. Materials and Methods

All the simulations in this work are performed by the Silvaco Victory Device code, which contains stress-dependent mobility and bandgap models, DC/AC and transient analysis, a high field saturation model, an SRH recombination model, a thermionic current model, a band gap narrowing model, and drift-diffusion and energy balance transport equations. This is a powerful advanced semiconductor device simulation tool featuring accurate modeling, scalability, support of multi-physics simulations, customizability, user-friendly interface, comprehensive process/device libraries, and efficient design optimization. The electric field distribution was obtained from the result of the simulations, and the breakdown voltage and location of the device were defined at the point of exceeding the critical electrical field of Ga_2O_3 (~ 8 MV/cm). The geometries and meshes were set up to simulate our experimental devices, whose fabrication has been described previously [25–27]. In brief, these are vertical geometry $\text{NiO}/\text{Ga}_2\text{O}_3$ rectifiers with bilayer NiO thickness of 10–70/10–70 nm and the length of the NiO extension beyond the top contact from 0 to 30 μm to form guard rings. The epitaxial layer structures consisted of a lightly doped drift layer with a thickness of 10 μm , grown by halide vapor phase epitaxy (HVPE) on a (001) Sn-doped (10^{19} cm^{-3}), bulk $\beta\text{-Ga}_2\text{O}_3$ single-crystal substrate. Full area backside Ohmic contacts were made using e-beam-evaporated Ti/Au followed by annealing at 550 $^\circ\text{C}$ for 180 s under N_2 . To prevent the early breakdown of the devices, it is important to use low-damage deposition conditions for the NiO bilayer that forms the heterojunction. In this case, it was deposited through rf (13.56 MHz) magnetron sputtering at 3 mTorr and subsequently annealed at 300 $^\circ\text{C}$ under O_2 [28]. Finally, a cathode contact of 20/80 nm Ni/Au (100 μm in diameter) was deposited onto the NiO layers. For comparison, we also fabricated metal Schottky rectifiers, which were the same in all respects but did not include the NiO layers. Figure 1 shows the schematics of the fabricated heterojunction devices. Experimentally we found that catastrophic device hard breakdown occurred either at the edge of the NiO extension, as shown in Figure 1b, or at the edge of the Ni/Au contact, as shown in Figure 1d. This was determined by the choice of doping and thickness of the NiO , as will be discussed below. We have previously reported that at high reverse voltages, the rectifiers showed formation of pits along the periphery of the Schottky contact. The pits are clearer after etch removal of the Au/Ni contact, with scanning electron microscopy images of these pits, which result from avalanche failure of the Ga_2O_3 under the high field generated at the edge of the rectifying contact [29].

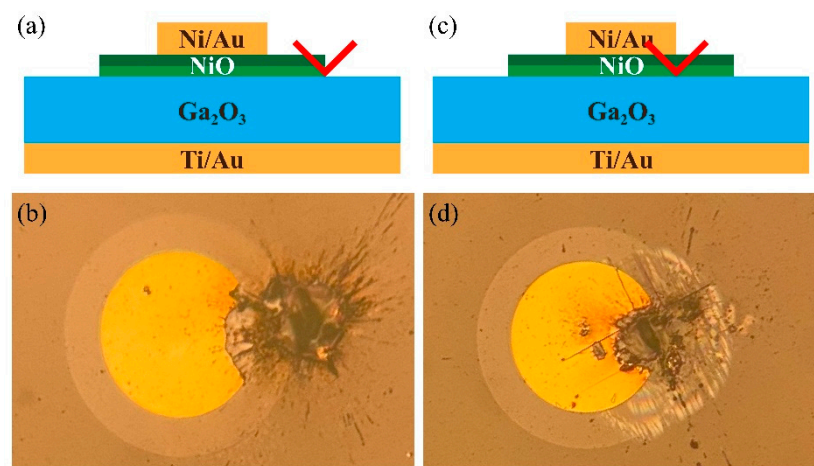


Figure 1. Schematics and optical microscope images of $\text{NiO}/\text{Ga}_2\text{O}_3$ heterojunction PN rectifier with breakdown location at the edge of (a,b) NiO and (c,d) anode metal contact. The dark green region is the high-doped NiO (10^{19} cm^{-3}), the light green region is the low-doped NiO (10^{18} cm^{-3}), while the Ga_2O_3 epitaxial layer thickness is 10 μm , grown on a conducting substrate of thickness $\sim 650 \mu\text{m}$. The layers in the schematics are not shown to scale.

3. Results and Discussion

The first simulation was to calculate the field distribution and breakdown voltage as a function of the top NiO layer thickness while holding the bottom layer constant at 10 nm. Figure 2a,b show the field distribution for two different NiO top layer thicknesses, demonstrating how the high field region can shift from the edge of the Ni/Au anode contact to the edge of the NiO extension. The 10 nm case has a better breakdown since the electric field was more effectively spread. The maximum electric field profile as a function of reverse bias for different top layer thicknesses is shown in Figure 2c. The maximum electric field in Ga₂O₃ does not fully increase with reverse bias. Instead, there is a flat region where the peak electric field shift from the edge of the guard ring to the edge of the metal contact. The device is considered to break down as soon as the peak electric field reaches its critical value (usually in the range of 4–8 MV/cm), which is determined by the crystal quality. As shown in Figure 2d, the breakdown voltage increases linearly with a thickness of up to 40 nm under a critical electric field of 8 MV/cm, and the breakdown was located at the edge of the NiO extension. However, at higher thicknesses, the maximum field location shifts back to the edge of the Ni/Au contact and occurs at a much lower reverse bias voltage. If the critical electric field is less than the commonly reported value of 8 MV/cm, the breakdown voltage becomes worse, and the best-performed thickness of the top NiO layer would also decrease. It should also be noted that the critical field is not precisely known for this material, and is based on theory, with most calculations implicitly assuming breakdown occurs when the applied electric field and depletion width are sufficiently high to create infinite charge multiplication. This analysis assumes that impact ionization is the breakdown mechanism, but this has never been experimentally verified in Ga₂O₃ and in any case, the impact ionization coefficients have not been measured either.

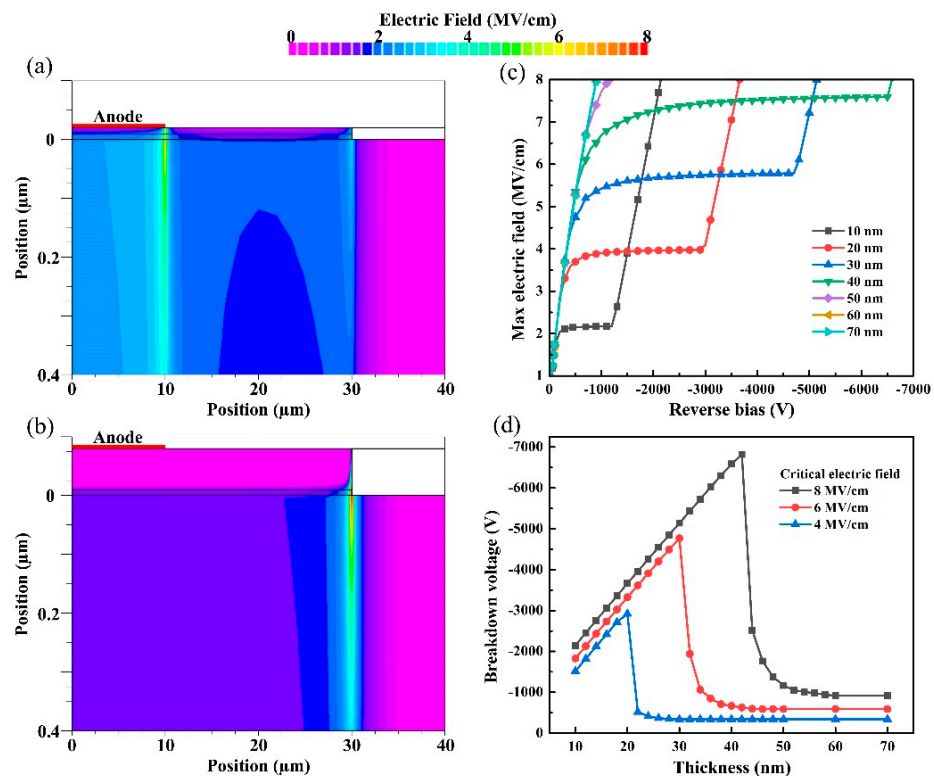


Figure 2. Electric field distribution of a device at the breakdown voltage with a NiO top layer thickness of (a) 10 nm, (b) 50 nm, (c) the maximum Ga₂O₃ electric field along the reverse bias until breakdown with various NiO top layer thicknesses, and (d) the correlation of breakdown voltage and NiO top layer thicknesses with the different critical electric fields.

Next, we examined how the breakdown region shifted with reverse bias, with all other conditions held constant. Figure 3a–c shows the electric field distributions under three different biases, while Figure 3d shows the spatial location of the peak electric field as a function of reverse bias. Although the peak electric field in Figure 3a,b has the same value and is at the same location, the field spreads back to the edge of the anode as the bias voltage increases. There exists a maximum electric field between the edge of the NiO and the edge of the anode which is determined by the thickness of the NiO (the flat region in Figure 2c). When this region is reached, the peak electric field will no longer increase at the edge of the NiO. Instead, the back-spreading peak electric field will fill out the space between the two edges and only when that space is saturated, the peak electric field will then start to ramp up at the edge of the metal contact. A video showing this transition of the electric field distribution as a function of time is shown in Figure S1 in the Supplemental File. In addition, the temporal change in the depletion region of the top NiO layer is also shown in Figure S2. The depletion width expands along with the reverse bias until the layer is fully depleted, at the exact same bias where the peak electric field starts to grow on the edge of the contact metal.

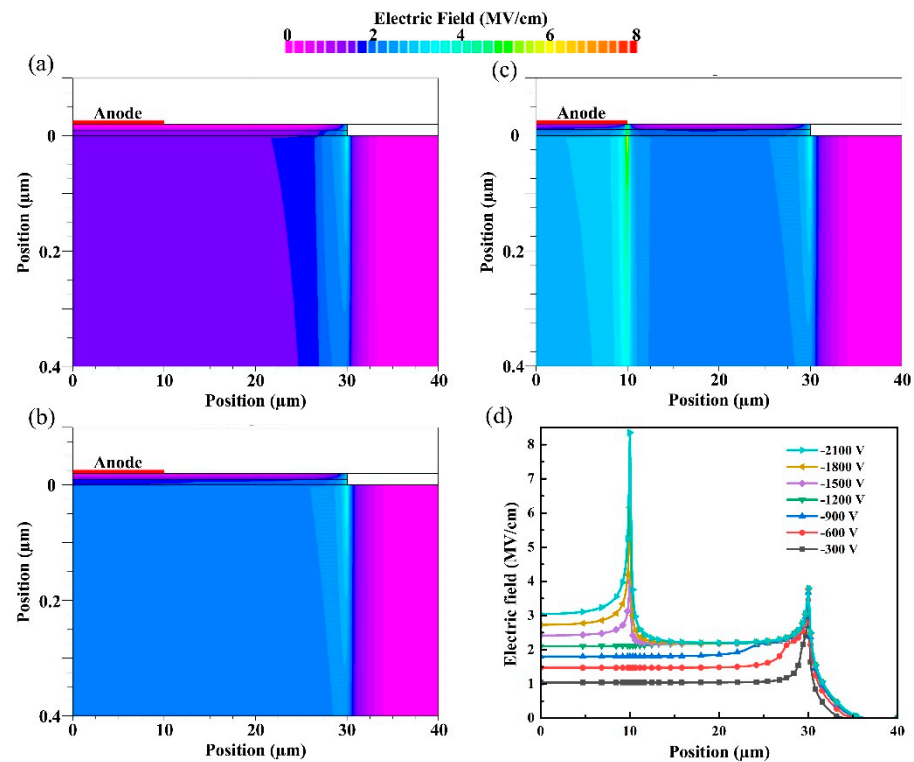


Figure 3. Electric field distribution of a device under the reverse bias of (a) -600 V, (b) -1200 V, (c) -1800 V, and (d) along the cutline at the PN junction.

Besides the thickness of the top NiO layer, the extension width of the guard ring is also a key component with regard to the device's breakdown performance. Figure 4a–c shows the electric field distribution at breakdown spreads out more as the top high-doped NiO layer extends away from the diode center. These three devices all have a fully depleted p-type layer when at breakdown, i.e., the peak electric field and breakdown are located at the edge of the anode metal contact. Moreover, there exists an optimized extension width considering the tradeoff between device area and breakdown performance, since Figure 4d shows that the breakdown voltage becomes saturated once the width of the top NiO layer extends further away, from 0 to $20\ \mu\text{m}$. In addition, the difference in breakdown voltage compared to a Schottky rectifier without the NiO contact is small when the guard ring is absent for these PN rectifiers.

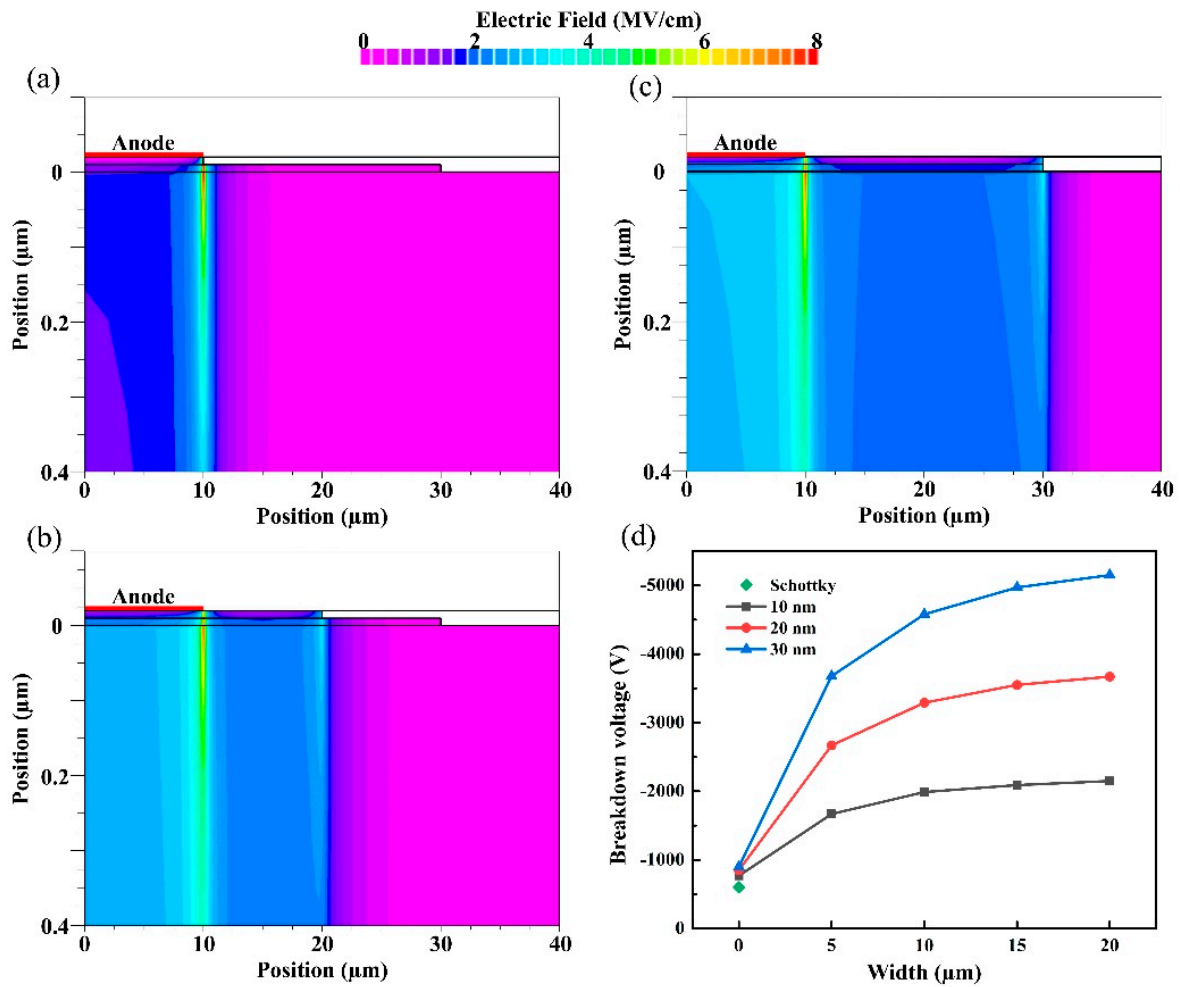


Figure 4. Electric field distribution of a device at the breakdown voltage with NiO top layer extension width of (a) 0 μm , (b) 10 μm , (c) 20 μm , and (d) their corresponding breakdown voltages with different top layer thickness.

The effect of varying the bottom low-doped layer of NiO on the device breakdown performance is also evaluated. In Figure 5a–c, the simulation results show that the electric field spreads out more as the low-doped bottom NiO layer thickness increases, a similar trend to the first region of varying the high-doped top NiO layer thickness. Figure 5d shows that the increase in breakdown voltage due to the bottom NiO thickness is irrelevant to the extension width of the top layer since the red and black curves have the same gap across the whole x -axis. Instead of varying the top layer of the NiO, the breakdown voltage is less “sensitive” when varying low-doped layer thickness. Compared with Figure 2d, we can see 70 nm of low-doped NiO has the same breakdown voltage as 20 nm of high-doped NiO. If we keep increasing the thickness of the bottom layer, a similar trend of a sudden drop in breakdown voltage as in the second region of Figure 2d is also seen.

The doping concentration of the NiO layer at the PN junction also played a significant role in device breakdown performances. Figure 6a–c shows that a higher doping concentration in the bottom layer of NiO leads to a higher breakdown voltage due to the more spread-out electric field distribution. This is consistent with the experimental result that higher-doped NiO layers have a higher breakdown field. Again, Figure 6d shows that the increase in breakdown voltage due to the bottom NiO doping concentration is irrelevant to the extension width of the top layer, since the red and black curves have the same gap across the whole x -axis.

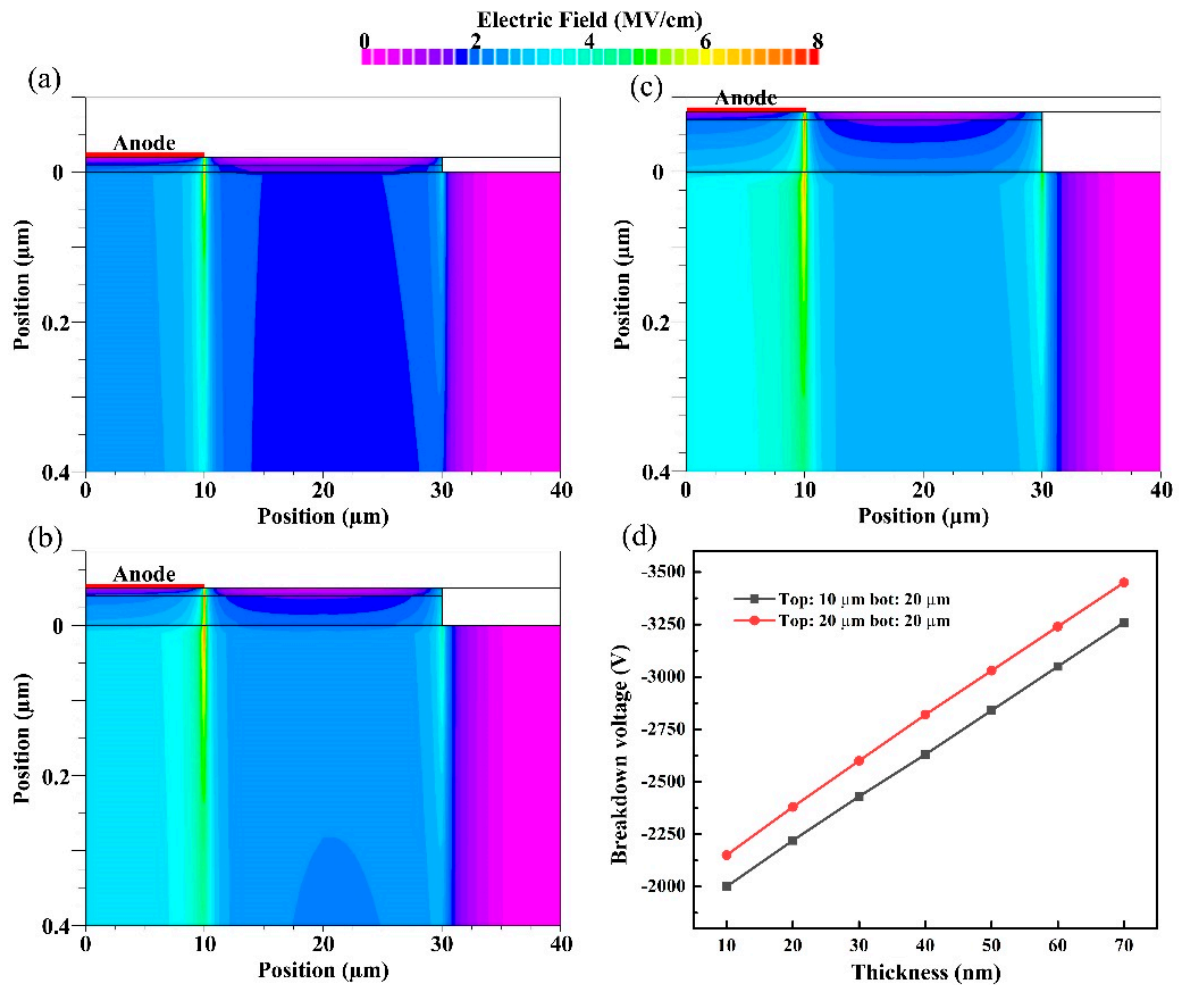


Figure 5. Electric field distribution of a device at the breakdown voltage with a NiO bottom layer thickness of (a) 10 nm, (b) 40 nm, (c) 70 nm, and (d) the correlation between NiO bottom layer thickness and breakdown voltage with two different extension widths of the top layer.

Since all the conditions in Figure 6 indicate a peak electric field at the edge of the anode contact, i.e., with a fully depleted NiO layer, a more detailed view of the electric field versus reverse bias voltage with a higher thickness of the bottom layer NiO should be further investigated. The simulated devices in Figure 7 all have structures with a bottom NiO layer of 200 nm. They show a similar trend as Figure 2c, which consists of two regions, one with a curve and one with a straight line. The correlation shown in Figure 6d is depicted again in Figure 8 with this thick bottom layer structure. This time, when the doping concentration is increased, there is a maximum in the curve at around 10^{18} cm^{-3} . When the doping concentration is less than 10^{18} cm^{-3} , the whole NiO layer is depleted at the breakdown voltage. Above 10^{18} cm^{-3} , the depletion width at breakdown starts to decrease along with the increasing concentration. The Supplemental File also contains an animation showing the depletion edges at breakdown while varying the doping concentration (Figure S3). When the device is in the first curved region of Figure 7, the depletion width is growing with the increasing reverse bias. And, if it breaks down at this moment due to any reason such as a low critical electric field, the breakdown location will be at the edge of the NiO. On the other hand, when the device is in the second linear region, the whole NiO is fully depleted and it would break down at the edge of the anode contact metal. Nonetheless, the final breakdown voltages depend on various parameters like the geometry (thickness/extension width), the doping concentration of the NiO layer, or the critical electric field of the Ga_2O_3 .

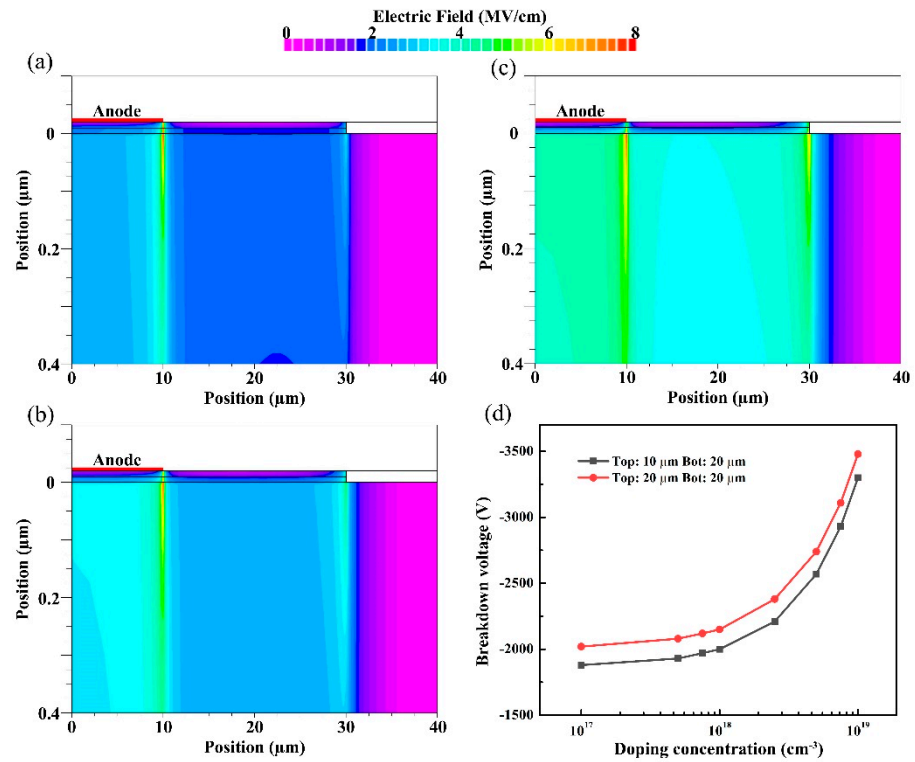


Figure 6. The electric field distribution of a device at the breakdown voltage with a NiO bottom layer doping concentration of (a) 1×10^{17} , (b) 5×10^{18} , (c) 1×10^{19} , and (d) the correlation between NiO bottom layer doping concentration and breakdown voltage with two different extension widths of the top layer.

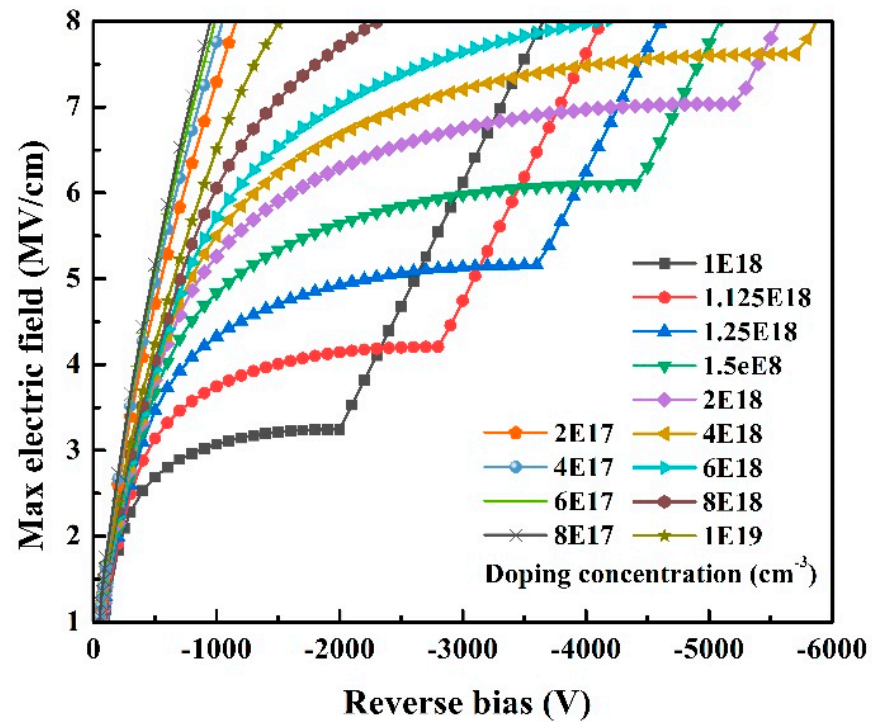


Figure 7. The correlation of the electric field and reverse bias voltage, with different NiO bottom layer (200 nm) doping concentrations from 10^{17} to 10^{19} cm⁻³.

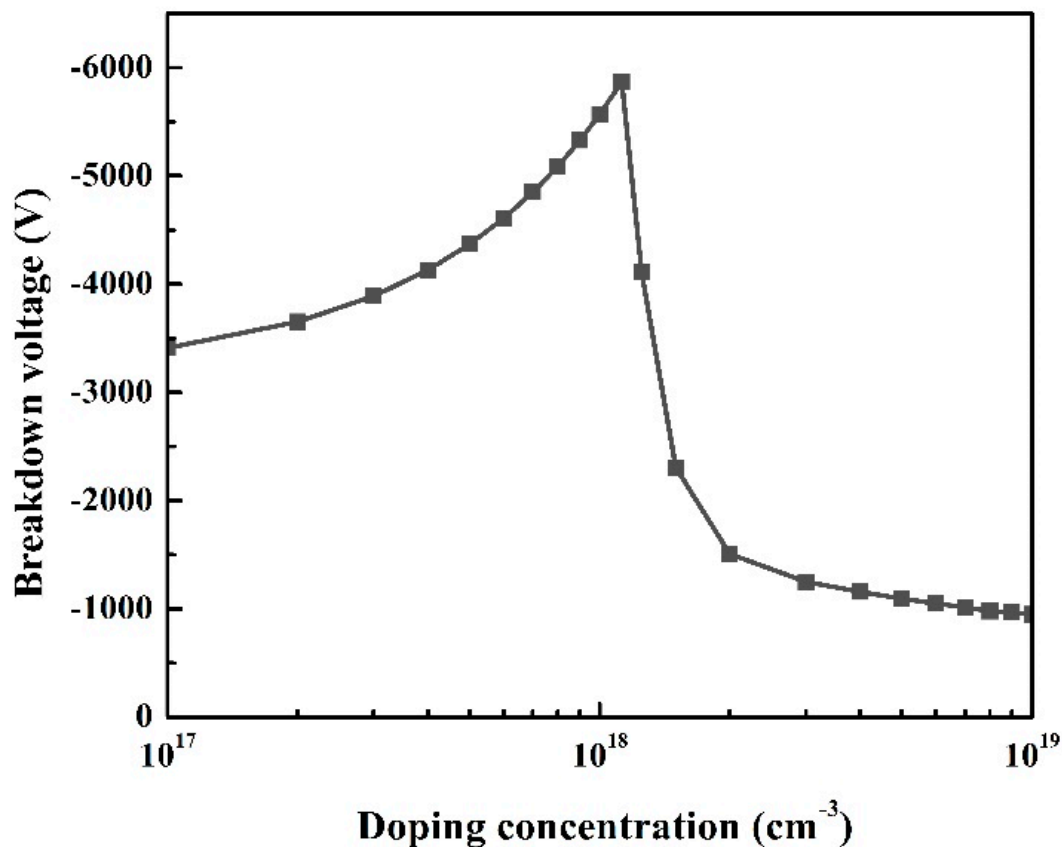


Figure 8. Breakdown voltage as a function of bottom NiO layer doping concentration.

4. Conclusions

The breakdown voltage and location in reverse-biased NiO/Ga₂O₃ rectifiers are found to be strongly dependent on the doping and thickness of the NiO and its extension beyond the top metal contact. The TCAD simulations show excellent agreement with the experimental observation that devices can suffer catastrophic damage at either the metal contact edge or at the end of the NiO extension. There are two different regions depending on the NiO parameters. When the device is operating in the first region, the depletion width initiates its growth. If a breakdown occurs during this stage, caused by factors such as a low critical electric field, the point of failure will be at the edge of the NiO material. When purposely driven to failure at high reverse bias, pits are observed in the high field regions at the edge of the contact or NiO extension regions. Conversely, in the second region, the entire NiO layer becomes fully depleted, and any breakdown would take place at the edge of the metal component. The Supplemental Material contains several visualization files showing these effects. The ultimate breakdown voltages are influenced by various parameters, including the geometry (thickness/width) and doping concentration of the NiO layer, as well as the critical electric field of the Ga₂O₃ material. It will also be interesting to see differences between the different Ga₂O₃ polymorphs. The various polymorphs of gallium oxide offer a wide range of properties and potential applications. α -Ga₂O₃ and β -Ga₂O₃, with their wide bandgaps, find applications in high-power electronics and deep ultraviolet optoelectronics, respectively. γ -Ga₂O₃'s narrow bandgap makes it promising for sensors and energy storage devices. Lastly, the less common ϵ -Ga₂O₃ shows potential in optoelectronics and solar cells. Further research and development in these different polymorphs will undoubtedly lead to exciting advancements in various fields and pave the way for new technological innovations.

Supplementary Materials: The following supporting information can be downloaded at: <https://www.mdpi.com/article/10.3390/cryst13071124/s1>, Figure S1: Animation showing temporal variation in electric field distribution. This is an animation of simulated heterojunction devices under reverse bias from -100 V to -2100 V. (the same structure from Figure 3 in the manuscript) There exists a maximum electric field between the edge of the NiO and the edge of the anode which is determined by the thickness of the NiO; Figure S2: Animation showing the movement of the depletion region (red line) during the conditions in Figure S1, i.e., the sweep of the bias from -100 V to -2100 V. The area is enlarged in the y-axis to focus on the depletion of the NiO layer; Figure S3: Animation showing the movement of the depletion region during the conditions in Figure 7 in the manuscript, i.e., changing the doping in the NiO at a fixed thickness of 200 nm.

Author Contributions: Conceptualization, F.R. and S.J.P.; methodology, C.-C.C. and F.R.; software, C.-C.C.; validation, J.-S.L., H.-H.W. and C.-C.C.; formal analysis, C.-C.C. and H.-H.W.; investigation, C.-C.C. and J.-S.L.; resources, F.R.; data curation, C.-C.C. and J.-S.L.; writing—original draft preparation, C.-C.C.; writing—review and editing, F.R. and S.J.P.; visualization, C.-C.C.; supervision, F.R.; project administration, F.R.; funding acquisition, F.R. All authors have read and agreed to the published version of the manuscript.

Funding: This research was funded by the Department of the Defense, Defense Threat Reduction Agency under award HDTRA1-20-2-0002. The work at UF was also supported by NSF DMR 1856662.

Data Availability Statement: The data that supports the findings of this study are available within the article.

Acknowledgments: The work at UF was performed as part of the Interaction of Ionizing Radiation with the Matter University Research Alliance (IIRM-URA), sponsored by the Department of the Defense, Defense Threat Reduction Agency under award HDTRA1-20-2-0002. The content of the information does not necessarily reflect the position or the policy of the federal government, and no official endorsement should be inferred. The work at UF was also supported by NSF DMR 1856662.

Conflicts of Interest: The authors declare no conflict of interest.

References

1. Green, A.J.; Speck, J.; Xing, G.; Moens, P.; Allerstam, F.; Gumaelius, K.; Neyer, T.; Arias-Purdue, A.; Mehrotra, V.; Kuramata, A. β -Gallium oxide power electronics. *APL Mater.* **2022**, *10*, 029201. [[CrossRef](#)]
2. Kokubun, Y.; Kubo, S.; Nakagomi, S. All-oxide p–n heterojunction diodes comprising p-type NiO and n-type β -Ga₂O₃. *Appl. Phys. Express* **2016**, *9*, 091101. [[CrossRef](#)]
3. Lu, X.; Deng, Y.; Pei, Y.; Chen, Z.; Wang, G. Recent advances in NiO/Ga₂O₃ heterojunctions for power electronics. *J. Semicond.* **2023**, *44*, 061802. [[CrossRef](#)]
4. Pearton, S.; Ren, F.; Tadjer, M.; Kim, J. Perspective: Ga₂O₃ for ultra-high power rectifiers and MOSFETS. *J. Appl. Phys.* **2018**, *124*, 220901. [[CrossRef](#)]
5. Sharma, S.; Zeng, K.; Saha, S.; Singiseti, U. Field-plated lateral Ga₂O₃ MOSFETs with polymer passivation and 8.03 kV breakdown voltage. *IEEE Electron. Device Lett.* **2020**, *41*, 836–839. [[CrossRef](#)]
6. Wang, C.; Zhang, J.; Xu, S.; Zhang, C.; Feng, Q.; Zhang, Y.; Ning, J.; Zhao, S.; Zhou, H.; Hao, Y. Progress in state-of-the-art technologies of Ga₂O₃ devices. *J. Phys. D Appl. Phys.* **2021**, *54*, 243001. [[CrossRef](#)]
7. Zhang, J.; Dong, P.; Dang, K.; Zhang, Y.; Yan, Q.; Xiang, H.; Su, J.; Liu, Z.; Si, M.; Gao, J. Ultra-wide bandgap semiconductor Ga₂O₃ power diodes. *Nat. Commun.* **2022**, *13*, 3900. [[CrossRef](#)]
8. Zhou, H.; Zeng, S.; Zhang, J.; Liu, Z.; Feng, Q.; Xu, S.; Zhang, J.; Hao, Y. Comprehensive study and optimization of implementing p-NiO in β -Ga₂O₃ based diodes via TCAD simulation. *Crystals* **2021**, *11*, 1186. [[CrossRef](#)]
9. Dong, P.; Zhang, J.; Yan, Q.; Liu, Z.; Ma, P.; Zhou, H.; Hao, Y. 6 kV/3.4 m Ω ·cm² vertical β -Ga₂O₃ Schottky barrier diode with BV 2/R on, sp performance exceeding 1-D unipolar limit of GaN and SiC. *IEEE Electron. Device Lett.* **2022**, *43*, 765–768. [[CrossRef](#)]
10. Gong, H.; Chen, X.; Xu, Y.; Ren, F.-F.; Gu, S.; Ye, J. A 1.86-kV double-layered NiO/ β -Ga₂O₃ vertical p–n heterojunction diode. *Appl. Phys. Lett.* **2020**, *117*, 022104. [[CrossRef](#)]
11. Gong, H.; Yu, X.; Xu, Y.; Chen, X.; Kuang, Y.; Lv, Y.; Yang, Y.; Ren, F.-F.; Feng, Z.; Gu, S. β -Ga₂O₃ vertical heterojunction barrier Schottky diodes terminated with p-NiO field limiting rings. *Appl. Phys. Lett.* **2021**, *118*, 202102. [[CrossRef](#)]
12. Gong, H.; Zhou, F.; Xu, W.; Yu, X.; Xu, Y.; Yang, Y.; Ren, F.-f.; Gu, S.; Zheng, Y.; Zhang, R. 1.37 kV/12 A NiO/ β -Ga₂O₃ heterojunction diode with nanosecond reverse recovery and rugged surge-current capability. *IEEE Trans. Power Electron.* **2021**, *36*, 12213–12217. [[CrossRef](#)]
13. Hao, W.; He, Q.; Zhou, X.; Zhao, X.; Xu, G.; Long, S. 2.6 kV NiO/Ga₂O₃ heterojunction diode with superior high-temperature voltage blocking capability. In Proceedings of the 2022 IEEE 34th International Symposium on Power Semiconductor Devices and ICs (ISPSD), Vancouver, BC, Canada, 22–25 May 2022; pp. 105–108.

14. Hao, W.; Wu, F.; Li, W.; Xu, G.; Xie, X.; Zhou, K.; Guo, W.; Zhou, X.; He, Q.; Zhao, X. Improved Vertical β -Ga₂O₃ Schottky Barrier Diodes With Conductivity-Modulated p-NiO Junction Termination Extension. *IEEE Trans. Electron. Devices* **2023**, *70*, 2129–2134. [[CrossRef](#)]
15. Li, J.-S.; Chiang, C.-C.; Xia, X.; Wan, H.-H.; Ren, F.; Pearton, S. 7.5 kV, 6.2 GW cm⁻² NiO/ β -Ga₂O₃ vertical rectifiers with on-off ratio greater than 1013. *J. Vac. Sci. Technol. A* **2023**, *41*, 030401. [[CrossRef](#)]
16. Li, J.-S.; Chiang, C.-C.; Xia, X.; Yoo, T.J.; Ren, F.; Kim, H.; Pearton, S. Demonstration of 4.7 kV breakdown voltage in NiO/ β -Ga₂O₃ vertical rectifiers. *Appl. Phys. Lett.* **2022**, *121*, 042105. [[CrossRef](#)]
17. Wang, Y.; Gong, H.; Lv, Y.; Fu, X.; Dun, S.; Han, T.; Liu, H.; Zhou, X.; Liang, S.; Ye, J. 2.41 kV Vertical P-NiO/n-Ga₂O₃ Heterojunction Diodes With a Record Baliga's Figure-of-Merit of 5.18 GW/cm². *IEEE Trans. Power Electron.* **2021**, *37*, 3743–3746. [[CrossRef](#)]
18. Xia, X.; Li, J.-S.; Chiang, C.-C.; Yoo, T.J.; Ren, F.; Kim, H.; Pearton, S. Annealing temperature dependence of band alignment of NiO/ β -Ga₂O₃. *J. Phys. D Appl. Phys.* **2022**, *55*, 385105. [[CrossRef](#)]
19. Xiao, M.; Wang, B.; Spencer, J.; Qin, Y.; Porter, M.; Ma, Y.; Wang, Y.; Sasaki, K.; Tadjer, M.; Zhang, Y. NiO junction termination extension for high-voltage (>3 kV) Ga₂O₃ devices. *Appl. Phys. Lett.* **2023**, *122*, 183501. [[CrossRef](#)]
20. Xu, G.; Wu, F.; Liu, Q.; Han, Z.; Hao, W.; Zhou, J.; Zhou, X.; Yang, S.; Long, S. Vertical β -Ga₂O₃ power electronics. *J. Semicond.* **2023**, *44*, 070301.
21. Yan, Q.; Gong, H.; Zhang, J.; Ye, J.; Zhou, H.; Liu, Z.; Xu, S.; Wang, C.; Hu, Z.; Feng, Q. β -Ga₂O₃ hetero-junction barrier Schottky diode with reverse leakage current modulation and BV²/Ron, sp value of 0.93 GW/cm². *Appl. Phys. Lett.* **2021**, *118*, 122102. [[CrossRef](#)]
22. Yan, Q.; Gong, H.; Zhou, H.; Zhang, J.; Ye, J.; Liu, Z.; Wang, C.; Zheng, X.; Zhang, R.; Hao, Y. Low density of interface trap states and temperature dependence study of Ga₂O₃ Schottky barrier diode with p-NiOx termination. *Appl. Phys. Lett.* **2022**, *120*, 092106. [[CrossRef](#)]
23. Zhou, F.; Gong, H.; Wang, Z.; Xu, W.; Yu, X.; Yang, Y.; Ren, F.-F.; Gu, S.; Zhang, R.; Zheng, Y. Over 1.8 GW/cm² beveled-mesa NiO/ β -Ga₂O₃ heterojunction diode with 800 V/10 A nanosecond switching capability. *Appl. Phys. Lett.* **2021**, *119*, 262103. [[CrossRef](#)]
24. Zhou, F.; Gong, H.; Xu, W.; Yu, X.; Xu, Y.; Yang, Y.; Ren, F.-F.; Gu, S.; Zheng, Y.; Zhang, R. 1.95-kV beveled-mesa NiO/ β -Ga₂O₃ heterojunction diode with 98.5% conversion efficiency and over million-times overvoltage ruggedness. *IEEE Trans. Power Electron.* **2021**, *37*, 1223–1227. [[CrossRef](#)]
25. Li, J.-S.; Chiang, C.-C.; Xia, X.; Wan, H.-H.; Ren, F.; Pearton, S. Effect of drift layer doping and NiO parameters in achieving 8.9 kV breakdown in 100 μ m diameter and 4 kV/4 A in 1 mm diameter NiO/ β -Ga₂O₃ rectifiers. *J. Vac. Sci. Technol. A* **2023**, *41*, 043404. [[CrossRef](#)]
26. Li, J.-S.; Chiang, C.-C.; Xia, X.; Wan, H.-H.; Ren, F.; Pearton, S. Superior high temperature performance of 8 kV NiO/Ga₂O₃ vertical heterojunction rectifiers. *J. Mater. Chem. C* **2023**, *11*, 7750–7757. [[CrossRef](#)]
27. Li, J.-S.; Wan, H.-H.; Chiang, C.-C.; Xia, X.; Yoo, T.J.; Kim, H.; Ren, F.; Pearton, S.J. Reproducible NiO/Ga₂O₃ Vertical Rectifiers with Breakdown Voltage > 8 kV. *Crystals* **2023**, *13*, 886. [[CrossRef](#)]
28. Li, J.-S.; Xia, X.; Chiang, C.-C.; Hays, D.C.; Gila, B.P.; Craciun, V.; Ren, F.; Pearton, S. Deposition of sputtered NiO as a p-type layer for heterojunction diodes with Ga₂O₃. *J. Vac. Sci. Technol. A* **2023**, *41*, 013405. [[CrossRef](#)]
29. Yang, J.C.; Fares, C.; Elhassani, R.; Xian, M.; Ren, F.; Pearton, S.J.; Tadjer, M.; Kuramata, A. Reverse Breakdown in Large Area, Field-Plated, Vertical β -Ga₂O₃ Rectifiers. *ECS J. Solid State Sci. Technol.* **2019**, *8*, Q3159. [[CrossRef](#)]
30. Yang, J.C.; Chaker Fares, C.; Ren, F.; Chen, Y.T.; Liao, Y.T.; Chang, C.W.; Lin, J.; Tadjer, M.; Smith, D.J.; Pearton, S.J.; et al. Switching behavior and forward bias degradation of 700 V, 0.2 A, β -Ga₂O₃ vertical geometry rectifiers. *ECS J. Solid State Sci. Technol.* **2019**, *8*, Q3028. [[CrossRef](#)]

Disclaimer/Publisher's Note: The statements, opinions and data contained in all publications are solely those of the individual author(s) and contributor(s) and not of MDPI and/or the editor(s). MDPI and/or the editor(s) disclaim responsibility for any injury to people or property resulting from any ideas, methods, instructions or products referred to in the content.